

# Efficient two step optimization for large embedded deformation graph based SLAM

Jingwei Song<sup>1</sup>, Fang Bai<sup>1</sup>, Liang Zhao<sup>1</sup>, Shoudong Huang<sup>1</sup> and Rong Xiong<sup>2</sup>

**Abstract**—Embedded deformation nodes based formulation has been widely applied in deformable geometry and graphical problems. Though being promising in stereo (or RGBD) sensor based SLAM applications, it remains challenging to keep constant speed in deformation nodes parameter estimation when model grows larger. In practice, the processing time grows rapidly in accordance with the expansion of maps. In this paper, we propose an approach to decouple nodes of deformation graph in large scale dense deformable SLAM and keep the estimation time to be constant. We observe that only partial deformable nodes in the graph are connected to visible points. Based on this fact, sparsity of original Hessian matrix is utilized to split parameter estimation in two independent steps. With this new technique, we achieve faster parameter estimation with amortized computation complexity reduced from  $O(n^2)$  to closing  $O(1)$ . As a result, the computation cost barely increases as the map keeps growing. Based on our strategy, computational bottleneck in large scale embedded deformation graph based applications will be greatly mitigated. The effectiveness is validated by experiments, featuring large scale deformation scenarios.

## I. INTRODUCTION

SLAM (Simultaneous Localization And Mapping) is a technique widely used in robotics for pose estimation and environment mapping. Based on the great achievements in rigid SLAM, considerable attention has been switched to SLAM in deformable scenarios. These include RGBD camera based deformable human body reconstruction and RGB camera based soft-tissue SLAM in Minimally Invasive Surgery (MIS). The key challenge in developing deformable SLAM is how to define and formulate deformation.

As an early stage of the topic, researchers assume deformation scenario is technically similar to SLAM in dynamic environment. By assuming a large amount of target features to be static, approaches like [1] and [2] were proposed, which extended this presumption, adopted conventional extended Kalman filter (EKF) SLAM and Parallel Tracking and Mapping (PTAM) by applying some thresholds to separate rigid and non-rigid feature points. More recent works based on ORB-SLAM [3] have been proposed and modified in [4] [5] [6] [7] [8]. The above researches show that extending traditional rigid SLAM to non-rigid scenarios is possible. However, without deformation modeling, map reconstruction based on this assumption inevitably leads to gaps within rigid

patches from different perspectives. Due to the assumption of roughly rigidity, the more extensive deformation of the environment, the larger gaps exist in the recovered map.

A better solution is to model the deformation. Recognizing map deformation modeling is vital and indeed many brilliant researches turn to the computer vision society for efficient deformation description. One of the most well-known and well-studied techniques is the Embedded Deformation (ED) [9], which was initially proposed for designing smooth character motions in cartoons. ED graph makes use of a sparsely interconnected scattered nodes with attributes of local rigid transformation. By mixing these local rigid transformations with weights, a global deformation is simulated in a discrete but smooth form. ED graph has been widely applied in RGBD and stereo SLAM [10] [11] and 3D human reconstructions [12] [13] (discrete hierarchical warp grid but very similar to ED graph) [14] [15] [16]. The ED graph based SLAM formulation is able to describe the deformation of the environment in addition to camera pose, which blossoms with the application like [12] [13] [14] [16] for human motion reconstruction and [11] for large scale SLAM in MIS.

In the meantime, for more challenging monocular equipments, Finite Element Method (FEM) [17] [18] and Structure from Template (SfT) [19] were proposed to simulate deformation. Both methods use a predefined grid or triangular mesh template to describe the soft-tissue. However, to the best of our knowledge, it is hard to apply these methods when the map is incrementally built and no complete real-time implementation has demonstrated how it will effectively be applied in large scenarios.

Overall, ED graph based formulation is the most applicable and widely used approach for modeling deformations. Numerous real-time dense SLAM systems have validated its effectiveness, particularly in batch scenarios, with fast sequential or parallel implementation. However, ED graph based formulation also comes with disadvantages and limitations. One major issue in ED graph is that when new observation is incorporated, the number of nodes increases dramatically, posing heavy computational burden. Little attention has been paid in the field of truncated signed distance function based 3D human reconstruction because the target size as well as map extent are predefined. State estimation and map updating are all confined within a volume. In more general cases, however, as reported in [11], when reconstructing geometry without a predefined volume, the environment size is unbounded due to the sharply growth of the graph, which eventually implies an amortized  $O(n^2)$  complexity with respect to the number of nodes in the

<sup>1</sup> Centre for Autonomous Systems, University of Technology, Sydney, P.O. Box 123, Broadway, NSW 2007, Australia

<sup>2</sup> State Key Laboratory of Industrial Control Technology and Institute of Cyber-Systems and Control, Zhejiang University, 38 Zheda Road, 310027 Zhejiang, China

Email: {jingwei.song; fang.bai}@student.uts.edu.au, rxiong@zju.edu.cn, {Liang.Zhao; Shoudong.Huang}@uts.edu.au

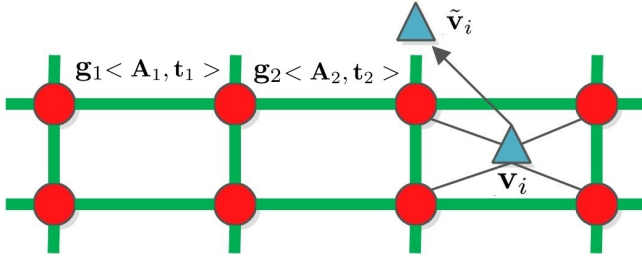


Fig. 1: A toy example of ED graph. The red circles are ED nodes, say node  $j$ , encoding a geometric position  $\mathbf{g}_j$ , and an affine transformation given by  $\mathbf{A}_j$  and  $\mathbf{t}_j$ . The blue triangle is a vertex, that can be deformed from  $\mathbf{v}_i$  to  $\tilde{\mathbf{v}}_i$ , through the impact of its neighboring ED nodes.

graph. In a word, optimizing an expanding ED graph in an unconstrained space significantly limits the performance of the system.

Even though little is known in speeding up ED graph based SLAM systems, numerous publications are dedicated into the graph based optimization in rigid scenarios. A typical graph optimization problem models robot poses (or landmark positions) as nodes in the graph, while the edges encode the relative measurement between connected nodes [20]. Graph sparsification is the most widely applied technique to marginalize subsets of nodes [21] [22] [23]. The key process in this topic is to sparsify edges and marginalize nodes based on indicators like divergence [23]. We will show in this paper that marginalization methods are of great value to enable efficiency in ED based SLAM. In this paper, we will solve the  $O(n^2)$  computational bottleneck encountered in the expanding environment, for ED graph based SLAM as reported in [11]. We analyze the spatial relationship between ED graph and observation and reveal the inherent sparsity pattern of Hessian matrix. Based on this discovery, we classify ED nodes into points relevant (PR) nodes and points irrelevant (PI) nodes and propose a decoupled optimization strategy.

In this work we extend ED graph research by converting the formulation into matrix form, which unveil a sparsity pattern that can be further exploited by restructuring the Jacobian matrix to benefit efficient marginalization. Based on this insight, we develop a method which split ED graph optimization into two steps and a lossy decoupled optimization strategy is proposed. The accuracy and effectiveness is tested on both the ED based geometry deformation as well as ED based SLAM application. The proposed strategy is validated on the MIS-SLAM [11] with and without the proposed strategy. For more background on this topic, please refer to flowchart of in [11].

## II. REVISIT GENERAL ED GRAPH BASED SLAM

Before embarking on this endeavor, let's first revisit structure of ED graph invented by [9] and see how to deform a target shape. Fig. 1 illustrates an example of ED graph. Nodes and their shared edges compose the ED graph. Each ED node  $j$  defines a local rigid motion modeled by  $\mathbf{A}_j, \mathbf{t}_j$ ,

where  $\mathbf{A}_j \in \mathbb{R}^{3 \times 3}$  is an affine matrix and  $\mathbf{t}_j \in \mathbb{R}^3$  is a translation vector. Given a random vertex  $\mathbf{v}_i$ , neighbouring ED nodes are chosen to contribute a deformation field defining how  $\mathbf{v}_i$  is deformed to its target position  $\tilde{\mathbf{v}}_i$ . Obviously, for a mesh based geometry, shape deformation is equivalent to translate vertices in the ED graph.

In practice, to avoid over-parameterization, the ED node positions  $\mathbf{g}_j$  are deliberately chosen to minimize the size of parameters. In researches like [9] [12] [14] [24], ED nodes are generated by uniformly downsampling the original model. The deformation between the point  $\mathbf{v}_i$  and  $\tilde{\mathbf{v}}_i$  is modeled as a transformation in the following form:

$$\tilde{\mathbf{v}}_i = \mathbf{R}_c \sum_{j=1}^m \omega_j(\mathbf{v}_i) [\mathbf{A}_j(\mathbf{v}_i - \mathbf{g}_j) + \mathbf{g}_j + \mathbf{t}_j] + \mathbf{T}_c, \quad (1)$$

where  $\mathbf{R}_c$  and  $\mathbf{T}_c$  are global rotation and translation relating to camera motion,  $m$  is the number of neighboring nodes. In the original framework [9], global camera pose  $\mathbf{R}_c$  and  $\mathbf{T}_c$  are not considered. However, the extensions with global movements, where the camera is not static, are provided in [12] [14] [24].  $\omega_j(\mathbf{v}_i)$  is a weight that quantifies the contribution of the ED node  $j$  to the vertex  $\mathbf{v}_i$ . We confine the number of nearest nodes to  $m = 4$  and define the weight in:

$$\omega_j(\mathbf{v}_i) = 1 - \|\mathbf{v}_i - \mathbf{g}_j\| / d_{max}, \quad (2)$$

where  $d_{max}$  is the maximum distance from the vertex  $\mathbf{v}_i$  to the neighbouring  $m$  nearest ED node.

Eq. (1) shows how one vertex is transformed with the ED graph. Conversely, if source ( $\mathbf{v}_i$ ) and target ( $\tilde{\mathbf{v}}_i$ ) point pairs are predefined, the parameters of ED graph ( $\mathbf{A}_j$  and  $\mathbf{t}_j$ ) can also be inferred. Thus, in the original ED graph as well as in ED graph based deformable SLAM, the problem is formulated as inferring ED graph parameter from a cluster of arbitrary source and target points pairs. Then, ED graph is applied to deform the whole model. To the best of our knowledge, all ED graph based SLAM systems consist of at least three terms: Rotation constraint, regularization constraint and a penalty term on the distance of deformed source and target point pairs. Some methods introduce more innovating terms, like visual hull term in [14], key features in [13] which are beyond the scope. The problem can be formulated by minimizing an energy function consists of three basic terms:

$$\underset{\mathbf{R}_c, \mathbf{T}_c, \mathbf{A}_1, \mathbf{t}_1, \dots, \mathbf{A}_m, \mathbf{t}_m}{\operatorname{argmin}} \omega_{rot} E_{rot} + \omega_{reg} E_{reg} + \omega_{data} E_{data}. \quad (3)$$

The major key point pairs matching term is  $E_{data}$ , while two soft constraints  $E_{rot}$  and  $E_{reg}$  avoid unreasonable deformation.  $E_{rot}$  hauls the affine matrix close to  $SO(3)$  by minimizing the following function of the column vectors  $\mathbf{c}_1, \mathbf{c}_2$  and  $\mathbf{c}_3$ :

$$E_{rot} = \sum_{j=1}^m \operatorname{Rot}(\mathbf{A}_j) \quad (4)$$

$$\mathbf{M}_{3m \times n} = \begin{bmatrix} \vdots & \vdots & \vdots & \vdots & \vdots \\ \omega_{i=\mathbb{N}(1,1)} * (v_1 - g_{i=\mathbb{N}(1,1)}) & \cdots & \cdots & \cdots & \cdots \\ \vdots & \vdots & \vdots & \vdots & \omega_{i=\mathbb{N}(n,1)} * (v_n - g_{i=\mathbb{N}(n,1)}) \\ \omega_{i=\mathbb{N}(1,2)} * (v_1 - g_{i=\mathbb{N}(1,2)}) & \cdots & \cdots & \cdots & \omega_{i=\mathbb{N}(n,2)} * (v_n - g_{i=\mathbb{N}(n,2)}) \\ \vdots & \vdots & \vdots & \vdots & \omega_{i=\mathbb{N}(n,3)} * (v_n - g_{i=\mathbb{N}(n,3)}) \\ \omega_{i=\mathbb{N}(1,3)} * (v_1 - g_{i=\mathbb{N}(1,3)}) & \cdots & \cdots & \cdots & \cdots \\ \vdots & \vdots & \vdots & \vdots & \vdots \\ \omega_{i=\mathbb{N}(1,4)} * (v_1 - g_{i=\mathbb{N}(1,4)}) & \cdots & \cdots & \cdots & \omega_{i=\mathbb{N}(n,4)} * (v_n - g_{i=\mathbb{N}(n,4)}) \\ \vdots & \vdots & \vdots & \vdots & \vdots \end{bmatrix} \quad (8)$$

$$\text{Rot}(\mathbf{A}) = (\mathbf{c}_1^T \cdot \mathbf{c}_2)^2 + (\mathbf{c}_1^T \cdot \mathbf{c}_3)^2 + (\mathbf{c}_2^T \cdot \mathbf{c}_3)^2 + (\mathbf{c}_1^T \cdot \mathbf{c}_1 - 1)^2 + (\mathbf{c}_2^T \cdot \mathbf{c}_2 - 1)^2 + (\mathbf{c}_3^T \cdot \mathbf{c}_3 - 1)^2. \quad (5)$$

Regularization is to limit the divergence of motion field exerted from neighboring nodes. As indicated in Fig. 1, the deformation of a vertex is the combination of rigid transformation from its connected neighboring nodes. To ensure smoothness of the deformed surface, the motion field generated from nodes should be consistent; otherwise, the deformed shape will be fragmented and distorted. This is a general practice named ‘as-rigid-as-possible’ [25] [26] widely used in the computer vision community.  $E_{reg}$  is defined in following form:

$$E_{reg} = \sum_{j=1}^m \sum_{k \in \mathbb{N}(j)} \alpha_{jk} \|\mathbf{A}_j(\mathbf{g}_k - \mathbf{g}_j) + \mathbf{g}_j + \mathbf{t}_j - (\mathbf{g}_k + \mathbf{t}_k)\|^2. \quad (6)$$

Similar to [9],  $\alpha_{jk}$  is defined as the overlap influence of the two ED nodes but in practice is set to 1.  $\mathbb{N}(j)$  denotes the set of all neighboring nodes connected to node  $j$ . Normally, the number of neighboring nodes is set to 4.

To solve geometrical model to frame registration, ‘back-projection’ formulation is proposed as a substitution to iterative closest point (ICP). They make full use of 2D depth image for fast convergence. Readers may refer to [14] [12] [9] [24]. For simplicity, we introduce the basic source and target key point pairs described by [9]. Let  $\mathbf{v}_i$  and  $\tilde{\mathbf{v}}_i$  be the arbitrary key source point and key target points. Normally predefined in interactive phase, these key points define how model is to be deformed like bending the head or stretching the arm. The goal is to minimize the distance of deformed point set to target point set:

$$E_{data} = \sum_{i=1}^n \|\mathbf{R}_c \sum_{j \in \mathbb{N}(i)} \omega_j(\mathbf{v}_i) [\mathbf{A}_j(\mathbf{v}_i - \mathbf{g}_j) + \mathbf{g}_j + \mathbf{t}_j] + \mathbf{T}_c - \tilde{\mathbf{v}}_i\|^2. \quad (7)$$

### III. EFFICIENT TWO STEP OPTIMIZATION

#### A. Matrix form of ED graph deformation

To fully exploit the structure we rewrite the data term Eq. (7) in a matrix form for the convenience of sparsity

analysis. Let’s consider a group of predefined key source points defined as  $\mathbf{P} = [\mathbf{v}_1 \dots \mathbf{v}_n]$  and  $\tilde{\mathbf{P}} = [\tilde{\mathbf{v}}_1 \dots \tilde{\mathbf{v}}_n]$  to be the key target points in the matrix form. According to Eq. (1), each point  $\mathbf{v}_i$  is deformed by its 4 neighboring nodes. Thus we define two matrix  $\mathbf{M}$  (Eq. (8)) and  $\mathbf{C}$  (Eq. (9)):

$$\mathbf{C}_{m \times n} = \begin{bmatrix} \vdots & \vdots & \vdots & \vdots & \vdots \\ \omega_{i=\mathbb{N}(1,1)} & \cdots & \cdots & \cdots & \cdots \\ \vdots & \cdots & \cdots & \cdots & \omega_{i=\mathbb{N}(n,1)} \\ \omega_{i=\mathbb{N}(1,2)} & \cdots & \cdots & \cdots & \omega_{i=\mathbb{N}(n,2)} \\ \vdots & \cdots & \cdots & \cdots & \omega_{i=\mathbb{N}(n,3)} \\ \omega_{i=\mathbb{N}(1,3)} & \cdots & \cdots & \cdots & \cdots \\ \vdots & \cdots & \cdots & \cdots & \cdots \\ \omega_{i=\mathbb{N}(1,4)} & \cdots & \cdots & \cdots & \omega_{i=\mathbb{N}(n,4)} \\ \vdots & \cdots & \cdots & \cdots & \cdots \end{bmatrix}. \quad (9)$$

where  $\mathbb{N}(i, j)$  ( $j = 1, 2, 3, 4$ ) is the set of neighboring node to point  $\mathbf{v}_i$ . In matrices  $\mathbf{M}$  and  $\mathbf{C}$ , note that non-zero elements are not aligned. Each column only has 4 non-zero elements (neighboring nodes). The sum of each column in matrix  $\mathbf{C}$  is 1 due to the topology of points to nodes. In Eq. (7), a source point  $\mathbf{v}_i$  is transformed by its 4 neighboring node making 4 non-zero elements in  $\mathbf{M}$  and  $\mathbf{C}$ . The sum of all weight  $\omega_j(\mathbf{v}_i)$  is 1. Note that different source points have different topology, thus the location of non-zero elements are not aligned well in each column. We arrange the parameters of ED nodes  $\mathbf{A}_i$  and  $\mathbf{t}_i$  in the following form:

$$\mathbf{A} = (\mathbf{A}_1 \quad \cdots \quad \mathbf{A}_m) \quad (10)$$

$$\mathbf{T} = (\mathbf{t}_1 + \mathbf{g}_1 \quad \cdots \quad \mathbf{t}_m + \mathbf{g}_m). \quad (11)$$

Then Eq. (7) takes the following form:

$$E_{data} = \|\mathbf{R}_c \cdot [\mathbf{A} \cdot \mathbf{M} + \mathbf{T} \cdot \mathbf{C}] + \mathbf{T}_c \otimes \mathbf{1} - \tilde{\mathbf{P}}\|_F^2. \quad (12)$$

where  $\otimes$  is the kronecker product.  $\mathbf{1}$  is  $1 \times n$  vector of ones. And  $\|\cdot\|_F^2$  is the Frobenius norm. Eq. (12) can be written compactly in the following form according to conclusions drawn from last section:

$$E_{data} = \|\mathbf{R}_c \cdot (\mathbf{A} \quad \mathbf{T}) \cdot \begin{pmatrix} \mathbf{M} \\ \mathbf{C} \end{pmatrix} + \mathbf{T}_c \otimes \mathbf{1} - \tilde{\mathbf{P}}\|_F^2. \quad (13)$$

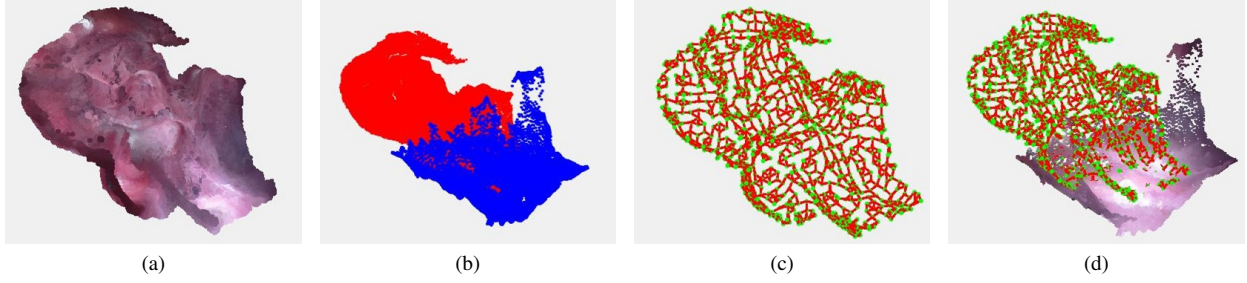


Fig. 2: Illustrated are the spatial relations of the visible points and the node graph. (a) is the latest reconstruction. (b) shows both the model (red) and the target depth (blue). (c) is the ED nodes and their edges. (d) presents the ED nodes and the target depth.

We define  $\mathbf{\Pi} = [\mathbf{M}^T \ \mathbf{C}^T]$  and  $\mathbf{\Phi} = [\mathbf{A} \ \mathbf{T}]^T$ . Therefore, Eq. (13) can be transformed to following formulation:

$$E_{data} = \|\mathbf{R}_c[\mathbf{\Pi}\mathbf{\Phi}]^T + \mathbf{T}_c \otimes \mathbf{1} - \tilde{\mathbf{P}}\|_F^2. \quad (14)$$

The property of Jacobian of  $E_{data}$  is determined by  $\mathbf{\Pi}$ .

### B. Sparsity in ED graph formulation

It is natural to solve Eq. (14) in a batch. As the number of vertices increases, the Jacobian relating to state  $\mathbf{\Phi}$  increase dramatically. Luckily, we explore the structure of  $\mathbf{\Pi}$  because only part of nodes are related to model points matching to observation. Fig. 2 indicates that the size of the depth image (blue points) is constant due to the limited field of view of the camera. The model keeps expanding while the target depth remains in small size. A typical ED node and target depth relationship is illustrated in Fig. 2(d); 2/3 of the nodes are not within range of target depth resulting no contribution to  $E_{data}$ . Fig. 3 shows a typical Jacobian of the cost function. In  $E_{data}$  block, shadow region indicates nodes connected to points (PR nodes) while zero block shows the nodes (PI nodes) free of any connected points. In this paper, we make full use of the sparsity of nodes in zero blocks.

The same sparsity also applies to Eq. (8) and Eq. (9). By rearranging matrix  $\mathbf{\Pi}$  from Fig. 3(a) to Fig. 3(b), we achieve a new Jacobian with zero block. Using this new matrix, Eq. (14) is rewritten to following form:

$$\begin{aligned} E_{data} &= \|\mathbf{R}_c[\mathbf{\Pi}\mathbf{\Phi}]^T + \mathbf{T}_c \otimes \mathbf{1} - \tilde{\mathbf{P}}\|_F^2 \\ &= \|\mathbf{R}_c\left[\begin{pmatrix} \mathbf{\Pi}' & \mathbf{0} \end{pmatrix} \begin{pmatrix} \mathbf{\Phi}_1 \\ \mathbf{\Phi}_2 \end{pmatrix}\right]^T + \mathbf{T}_c \otimes \mathbf{1} - \tilde{\mathbf{P}}\|_F^2, \end{aligned} \quad (15)$$

where  $\mathbf{\Phi}_1$  is the  $\mathbf{A}_j$  and  $\mathbf{t}_j$  of PR node set and  $\mathbf{\Phi}_2$  is the  $\mathbf{A}_j$  and  $\mathbf{t}_j$  of PI node set.  $\mathbf{\Pi}'$  is the subset of  $\mathbf{\Pi}$  relating to PR nodes (shadow region in Fig. 2).

### C. Lossy Two level optimization

Explained in Section III-B, the size of the PR nodes is almost constant due to the limited size of depth image in scenario when map keeps expanding. For instance, the point cloud generated from Hamlyn dataset [27] (grabbed from monitor) is only  $320 \times 240 = 76800$  at most. **As the**

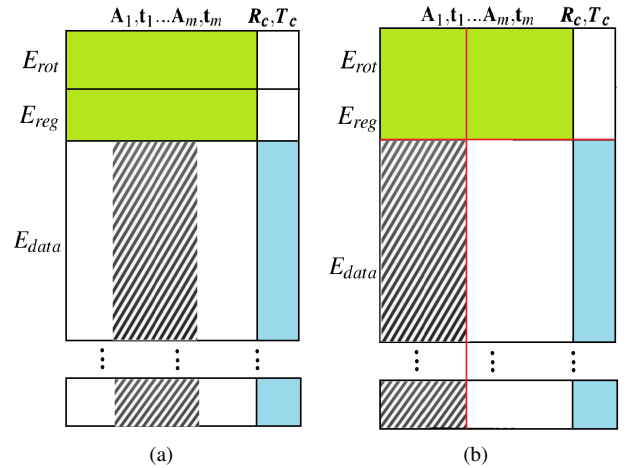


Fig. 3: (a) is an example of Jacobian. Empty block means the element in this block are zero. (b) is re-ordered Jacobian.

**model grows, the total number of nodes in ED graph is increasing but the number of PR nodes is almost constant.**

Taking advantage of Eq. (15), the optimization can be divided into two levels: the optimization of PR nodes  $\mathbf{\Phi}_1$  and the optimization of the rest PI nodes  $\mathbf{\Phi}_2$ .

Therefore, we first optimize  $(\mathbf{\Phi}_1, \mathbf{R}_c$  and  $\mathbf{T}_c)$  by fixing  $\mathbf{\Phi}_2$  in (**Level I**) optimization, to obtain an estimation of the three parameters  $\mathbf{\Phi}_1, \mathbf{R}_c$  and  $\mathbf{T}_c$ . Then the value of the parameters obtained from level I, will be fixed in **Level II**, together with the two soft constraints  $E_{rot}$  and  $E_{reg}$  to optimize the parameter  $\mathbf{\Phi}_2$ . We explicitly enforce this idea by formulating following energy function:

$$\operatorname{argmin}_{\mathbf{R}_c, \mathbf{T}_c, \mathbf{\Phi}_1} \omega_{rot}\tilde{E}_{rot} + \omega_{reg}\tilde{E}_{reg} + \omega_{data}E_{data} \quad (16)$$

$$\operatorname{argmin}_{\mathbf{\Phi}_2} \omega_{rot}E_{rot} + \omega_{reg}E_{reg} \quad (17)$$

Eq. (16) and Eq. (17) are the **Level I** and **Level II** energy functions, where  $\tilde{E}_{rot}$  and  $\tilde{E}_{reg}$  are the subset of energy function of  $E_{rot}$  and  $E_{reg}$  containing  $\mathbf{\Phi}_1$ . In other words, the size of Eq. (16) is only related to the size of PR nodes.

Therefore, the computational complexity in optimizing **Level I** is reduced from  $O(n^2)$  to constant  $O(1)$  thanks to the constant size of  $\Phi_1$ . Undoubtedly, optimizing **Level II** is still  $O(n^2)$ , but considering the scale of data term  $E_{data}$  is far larger than the rest, the computational cost in **Level II** is much smaller. Note that the new strategy keeps time consuming step **Level I** constant while **Level II** still  $O(n^2)$ . **But the size of Level II is almost negligible comparing with Level I.**

#### D. Connection with Marginalization and Information Loss

In this section, we will draw the connection of the proposed two level optimization method with an exact marginalization based method. The analysis will show that the information loss is very low, illustrating the feasibility of the decoupled optimization Eq. (16) and Eq. (17).

When generating Eq. (15), the Jacobian shown in Fig. 3 is re-ordered by classifying  $[\mathbf{A}_1, \mathbf{t}_1 \dots \mathbf{A}_m, \mathbf{t}_m]$  into PR nodes set  $\Phi_1$  and PI nodes set  $\Phi_2$ . The state in cost function  $[\mathbf{R}_c, \mathbf{T}_c, \mathbf{A}_1, \mathbf{t}_1 \dots \mathbf{A}_m, \mathbf{t}_m]$  are classified as  $\mathbf{x}_c(\mathbf{R}_c, \mathbf{T}_c, \mathbf{A}_1, \mathbf{t}_1 \dots \mathbf{A}_k, \mathbf{t}_k)$  and  $\mathbf{x}_f(\mathbf{A}_{k+1}, \mathbf{t}_{k+1} \dots \mathbf{A}_m, \mathbf{t}_m)$ . Fig. 3 shows the Jacobian in the new order. The first two term are combined due to their sparsity because  $E_{rot}$  and  $E_{reg}$  are node-wise and are unrelated to source points. The only full block in Fig. 3 is  $E_{data}$  with regard to  $\Phi_1$  (shadow region), specifically  $\frac{\partial \mathcal{J}_2}{\partial \mathbf{x}_c}$ . Let us write down the Jacobian and Hessian as,

$$\mathcal{J} = \begin{bmatrix} \frac{\partial \mathcal{J}_1}{\partial \mathbf{x}_c} & \frac{\partial \mathcal{J}_1}{\partial \mathbf{x}_f} \\ \frac{\partial \mathcal{J}_2}{\partial \mathbf{x}_c} & \mathbb{O} \end{bmatrix} \stackrel{\text{def}}{=} \begin{bmatrix} \mathbf{J}_{1c} & \mathbf{J}_{1f} \\ \mathbf{J}_{2c} & \mathbb{O} \end{bmatrix} \quad (18)$$

$$\mathcal{H} = \begin{bmatrix} \mathbf{J}_{1c}^T \mathbf{J}_{1c} + \mathbf{J}_{2c}^T \mathbf{J}_{2c} & \mathbf{J}_{1c}^T \mathbf{J}_{1f} \\ \mathbf{J}_{1f}^T \mathbf{J}_{1c} & \mathbf{J}_{1f}^T \mathbf{J}_{1f} \end{bmatrix} \stackrel{\text{def}}{=} \begin{bmatrix} \Lambda_{cc} & \Lambda_{cf} \\ \Lambda_{cf}^T & \Lambda_{ff} \end{bmatrix} \quad (19)$$

Obviously, the density of  $\frac{\partial \mathcal{J}_2}{\partial \mathbf{x}_c}$  makes  $\Lambda_{cc}$  the only dense block among Hessian  $\mathcal{H}$ . Taking this advantage we use marginalization technique [20] from classic rigid SLAM and separate the optimization in following form:

$$\begin{bmatrix} \Lambda_{cc} & \Lambda_{cf} \\ \Lambda_{cf}^T & \Lambda_{ff} \end{bmatrix} \begin{bmatrix} \mathbf{x}_c \\ \mathbf{x}_f \end{bmatrix} = \begin{bmatrix} \mathbf{J}_{1c}^T \mathbf{F} + \mathbf{J}_{2c}^T \mathbf{F} \\ \mathbf{J}_{1f}^T \mathbf{F} \end{bmatrix} \stackrel{\text{def}}{=} \begin{bmatrix} \mathbf{y}_c \\ \mathbf{y}_f \end{bmatrix} \quad (20)$$

$$\begin{bmatrix} \Lambda_{cc} - \Lambda_{cf} \Lambda_{ff}^{-1} \Lambda_{cf}^T & \mathbb{O} \\ \Lambda_{cf}^T & \Lambda_{ff} \end{bmatrix} \begin{bmatrix} \mathbf{x}_c \\ \mathbf{x}_f \end{bmatrix} = \begin{bmatrix} \mathbf{y}_c - \Lambda_{cf} \Lambda_{ff}^{-1} \mathbf{y}_f \\ \mathbf{y}_f \end{bmatrix} \quad (21)$$

After enforcing Schur complement, we successfully achieve only solving  $\mathbf{x}_c$  independent of  $\mathbf{x}_f$ . The computation of  $\mathbf{x}_c$  (including  $\mathbf{R}_c$ ,  $\mathbf{T}_c$  and  $\Phi_1$ ) is constant (explained in Section III-C). After solving  $\mathbf{x}_c$ , the optimization of  $\mathbf{x}_f$  is in tiny computation as the  $\Lambda_{ff} = (\frac{\mathbf{J}_{1f}}{\partial \mathbf{x}_f})^T (\frac{\mathbf{J}_{1f}}{\partial \mathbf{x}_f})$  and is only related to  $E_{rot}$  and  $E_{reg}$ . The sparsity of Hessian and small number of nodes ( $n \gg m$ ) makes the time of solving  $\mathbf{x}_f$  much less.

Fig. 4 is the Jacobian of  $E_{rot}$  and  $E_{reg}$  relating to all nodes. The first term  $E_{rot}$  is the sum error of affine transformation (Eq. (4)) making the Jacobian strictly diagonal. The second term  $E_{reg}$  defines the transformation error

within node and its neighbors (Eq. (6)). The major part  $\mathbf{A}_j(\mathbf{g}_k - \mathbf{g}_j) + \mathbf{g}_j + \mathbf{t}_j$  is also within one node  $j$  except the very last  $-(\mathbf{g}_k + \mathbf{t}_k)$ . The last variable  $\mathbf{t}_k$  makes the Jacobian not strictly diagonal (refer to Fig. 4(b)). We come up with an idea that by ignoring Jacobian of  $\mathbf{t}_k$ , and reordering two diagonal Jacobians, the combination  $[\frac{\partial \mathcal{J}_1}{\partial \mathbf{x}_c} \quad \frac{\partial \mathcal{J}_1}{\partial \mathbf{x}_f}]$  becomes diagonal and  $\Lambda_{cf} = (\frac{\partial \mathcal{J}_1}{\partial \mathbf{x}_c})^T (\frac{\partial \mathcal{J}_1}{\partial \mathbf{x}_f}) = 0$ . In this case, Eq. (20) can be separated into two equations, with respect to  $\mathbf{x}_c$  and  $\mathbf{x}_f$  respectively, which also correspond to the Level I and Level II of the proposed method. In a word, our two level lossy method can be considered as an approximation of Eq. (21), under the assumption that  $\Lambda_{cf} = 0$  roughly stands.

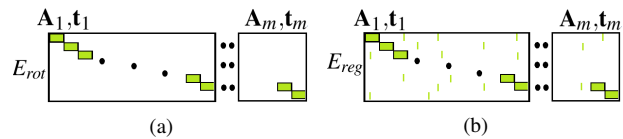


Fig. 4: (a) is Jacobian of  $E_{rot}$  with regard to all nodes. (b) is Jacobian of  $E_{reg}$  with regard to all nodes.

Fig. 5 visualizes the feasibility of the lossy decoupled optimization approach in geometry. PR nodes (green) are the only nodes that's connected to visible points and contribute to  $E_{data}$ . All PI nodes (purple) merely share edges with PR nodes and are passively deformed according to the behaviors of PR nodes. Equivalently, the inter-nodes relations in the Jacobian of  $E_{reg}$  (Fig. 4(b)) shows these connections (Fig. 4(b)). In view of this, our lossy decoupled optimization approach first optimize PR nodes and then estimate PI nodes.

**In conclusion, solving energy function Eq. (3) by first enforcing ignoring Jacobian of  $\mathbf{t}_k$  is equivalent to the proposed decoupled optimization in Eq. (16) and Eq. (17).**

The information loss of the proposed approach is relatively low. Fig. 5 illustrates the connection between PR nodes and

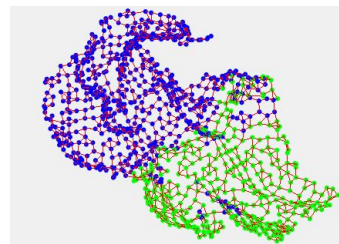


Fig. 5: Two types of nodes and edges. Green nodes are the PR nodes and purple nodes are PI nodes.

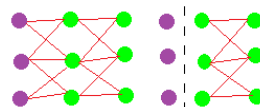


Fig. 6: Connections of PI (purple) and PR (green) nodes. Left is the full connection while the PI and PR connections are cut in our **Level I** optimization

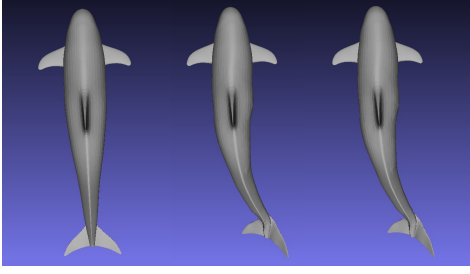


Fig. 7: Qualitative comparisons of our strategy and original ED based deformation. The first shape is the original dolphin mesh. We show the result of deformed shape (the last) along with the result of classical ED deformation (middle).

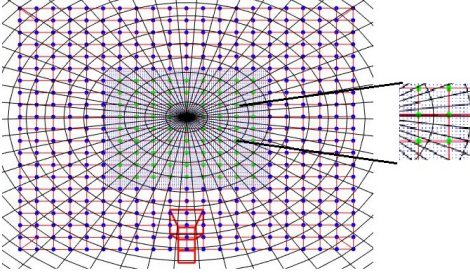


Fig. 8: A toy model. One step optimization step from plain visible surface model (tiny dots) to warped surface (grid). PI nodes are in blue and PR nodes are in green. Camera remains static.

PI nodes is weak on the boundary, in contrast with the dense connections among PR nodes. Fig. 6 demonstrates how the connection between PR and PI nodes are removed in **Level I** optimization. Correspondingly, the connection between  $\frac{\partial \mathbf{J}_1}{\partial \mathbf{x}_c}$  and  $\frac{\partial \mathbf{J}_1}{\partial \mathbf{x}_f}$  are removed resulting in  $\Lambda_{cf} = (\frac{\partial \mathbf{J}_1}{\partial \mathbf{x}_c})^T (\frac{\partial \mathbf{J}_1}{\partial \mathbf{x}_f}) = \mathbf{0}$ . The information between two PR nodes is strong while that among the PI nodes is weak. The weak information is neglected in **Level I**, attributing to relatively low information loss in optimization process.

#### IV. RESULTS AND DISCUSSION

Our goal is to have both qualitative assessments as well as quantitative comparisons between the original ED graph optimization and the proposed method. For qualitative comparison, we show the sacrificed accuracy has few impacts on final reconstructed map. A dolphin model is downloaded from turbosquid (<https://www.turbosquid.com>) for qualitative comparison. With regard to quantitative test in SLAM, both methods are compared on a tiny synthetic

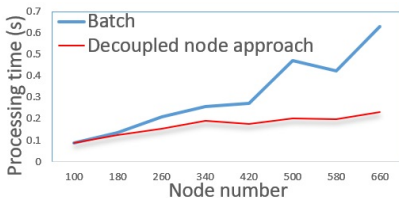


Fig. 9: Test results relating to Fig. 8.

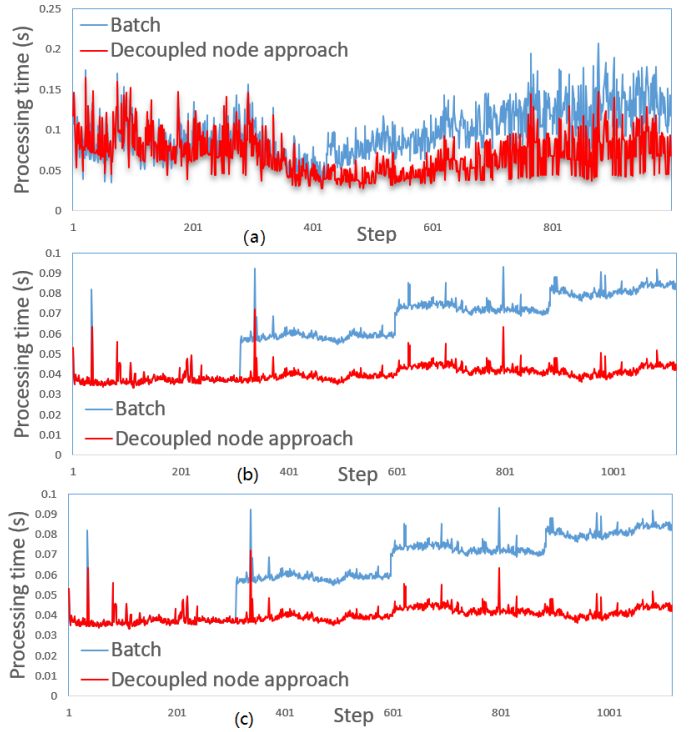


Fig. 10: Processing time comparisons of model 6 (a), 20 (b) and 21 (c) in Hamlyn dataset. Blue lines are the batch optimization and red lines are our nodes decoupled optimization. We cannot illustrate **Level I** and **Level II** separately due to time consumption of **Level II** is extremely low.

dataset and datasets from the Hamlyn Centre for Robotic Surgery [27], where we choose three in-vivo stereo videos with deformation and rigid scope movement. Other videos either have no deformation or scope motion. The frame rate and size of in-vivo porcine dataset (model 1) is 30 frame per second and  $640 \times 480$  while the other two is 25 frame per second and  $720 \times 288$ . Distance from camera to surface of soft-tissue is between 40 to 70 mm. The experiments are conducted on the same hardware and software environment of MIS-SLAM [24]. The module of state estimation in MIS-SLAM [24] is modified to the proposed approach. Note that an iterative solver, i.e. the preconditioned conjugate gradient method, is employed to solve the resulting linear systems, as it provides a way of parallel computing on GPU. Section IV-A shows the qualitative comparisons while the rest shows time complexity as well as the accuracy.

#### A. Qualitative ED deformation comparisons

Fig. 7 demonstrates the comparisons of ED graph deformed dolphin (middle) and the proposed approach (right). This comparison is not aiming as a proof of the superiority of the proposed method over the original ED graph method. [9] has already claimed real-time implementation on CPU as well as very nice results. Aiming at speeding up deformable SLAM application, the qualitative result of our lossy decoupled approach is not comparable to batch estimation of ED. However, we want to illustrate that the proposed method

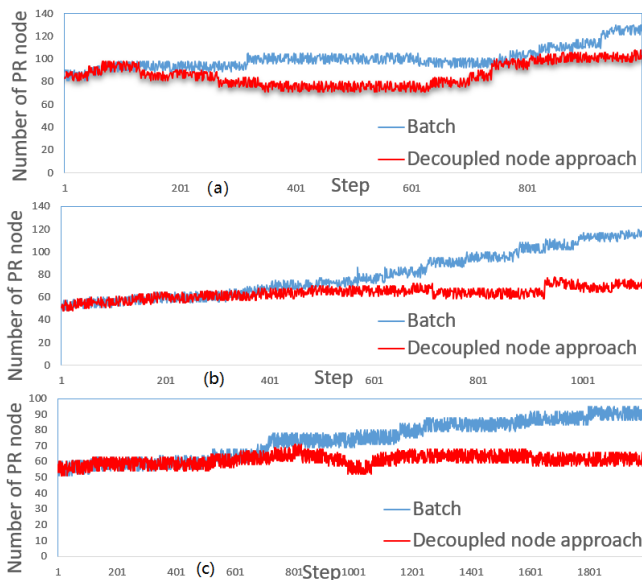


Fig. 11: Optimizing nodes comparisons in first level computation of model 6 (a), 20 (b) and 21 (c) in Hamlyn dataset. The red lines are the result of our decoupled optimization strategy while the blue lines are the original batch strategy.

can achieve similar result and the difference is not visible to the naked eye or difficult to make out. Fig. 7 confirms that the deformed shape performed by our approach do actually have similar result. The result looks very close to original ED graph partially due to simple topology of dolphin. Other complex model like human results in a visible but not very apparent difference. Although the decoupled optimization normally works well, the results can be much worse than ED when the nodes are too sparse. The deformation is dependent on PR nodes involved and the insufficiency of PR nodes (or nodes in conventional one step ED) causes vertex deformation that the expected target is not reached.

### B. Time complexity comparisons

Fig. 8 and Fig. 9 show a tiny one-step toy simulation and the result. Tractable time consumption remains small because PR node does not change.

We compare the original MIS-SLAM [24] with the improved version. Fig. 10 illustrates the running time for three Hamlyn datasets (model 6, 20 and 21). In all scenarios decoupled optimization yields better efficiency than batch processing especially in case of long term process (the last dataset in Fig. 10). In first few steps, robot is steady and ED graph is not expanding significantly. This attributes to similar processing time in first few hundred steps. When robot moves, the ED graph expands intensively and processing time increases abruptly in state optimization. In view of this, by limiting the size of node graph, decoupled optimization keeps time consumption stable due to the constant PR node scale.

From the demo video attached, readers will find the range of movement in model 6 is much smaller than model 20 and 21. That’s the main reason our method doesn’t contribute

greatly to model 6. However, as the environment gets larger, our approach keeps much lower time consumption.

Fig. 11 also shows the number of decoupled nodes. Our algorithm significantly keeps the **Level I** tractable. Note that we don’t present the time for **Level I** and **Level II** separately because the time consumption of **Level II** is only a few percent of **Level I**. Normally the size of energy function for **Level I** is 15000 to 40000 while there are only 500 to 1500 for **Level II** optimization. Based on the test on GPU, the time consumption of a typical **Level I** is 0.1 second while **Level II** is around 0.003 second.

### C. Accuracy comparisons

The lossy decoupled optimization strategy inevitably attributes the loss of accuracy. Section IV-A shows the quality of deformed map is well preserved in ED deformation process. Moreover, we compare the optimization performance of the lossy formulation and the original one on the same parameters and weights of terms in SLAM application (MIS-SLAM). Different from arbitrary key points matching in ED deformation formulation (Eq. (7)), in SLAM application the  $E_{data}$  term is in the form of model-to-depth scan matching like point-to-plane ICP. For quantitative validation, we measure the point-to-point distance of deforming map and target scan. For direct validation to ground truth, three synthetic data (heart, right kidney and stomach) are generated by deliberately deforming models from CT scanned phantom. We compare the error from the reconstruction to ground truth. As compliment, the three laparoscopy datasets from Hamlyn are tested, but only the back-projection error in each iteration is available since there’s no ground truth. In the batch approach, the average distance of back-projection registration of the three simulation scenarios are 0.18mm (model 6), 0.13mm (model 20) and 0.12mm (model 21). While dataset with ground truth (Hamlyn dataset 10/11) achieves 0.08mm, 0.21mm (Average errors). With our decoupled optimization approach, we achieve 0.31mm (model 6), 0.26mm (model 20), 0.22mm (model 21) and 0.14mm, 0.29mm errors. In the attached video, there is no big difference in terms of structure and texture.

Fig. 12 illustrates the average error of model to ground truth. On top of ground truth in Hamlyn dataset, we generate several synthetic datasets with ground truth. Please refer to attached video for more details of synthetic data. Roughly speaking, the proposed method sacrifices 32% (Fig. 12) accuracy in exchange for 50% speed gains (Fig. 11).

## V. CONCLUSION

We propose a novel two level deformation node decoupling approach that supports faster computation and reduces computational complexity from  $O(n^2)$  to near  $O(1)$ . The decoupled optimization structure achieves faster computation in scenario of expanding environment. Our strategy sacrifice small amount of accuracy in exchange of near constant processing speed. The constant computation complexity of the lossy strategy should have great potential for applications in ED graph based SLAM in unbounded map scenario.

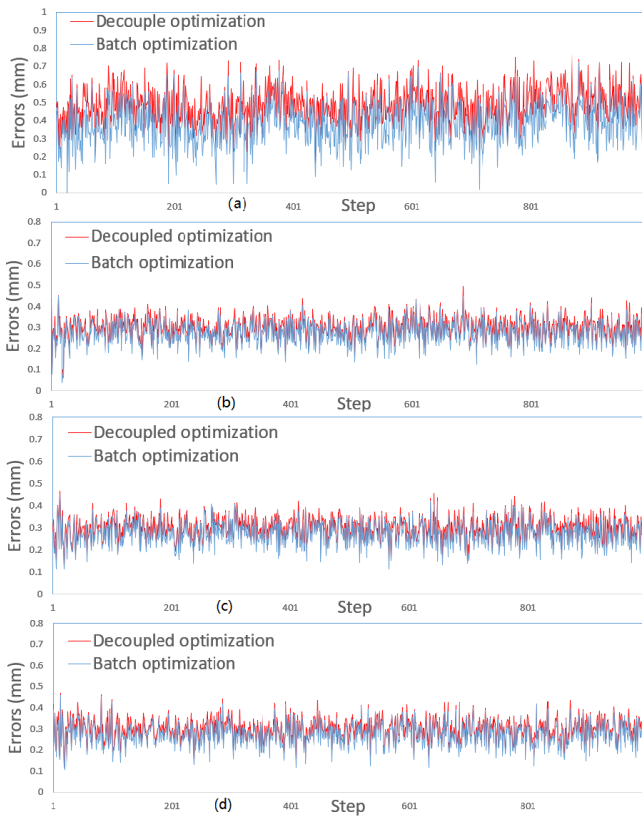


Fig. 12: Mean average error of 3D reconstruction (mm). From the first to last are Hamlyn dataset with ground truth, our synthetic heart, synthetic left kidney and synthetic stomach. Please refer to attached video for the synthetic data.

The node marginalization strategy in this paper, however, is straightforward and arbitrary which only classify nodes based on the node-vertex connectivity. It's reasonable because different from pose graph, ED graph is paralleled in GPU and time consumption requirement is more strict. However, it remains to be of great interest to test if pose graph pruning method like KullbackLiebler divergence minimization outperforms the proposed work while remains tiny consumption in GPU environment.

## REFERENCES

- [1] O. G. Grasa, J. Civera, and J. Montiel, "EKF monocular slam with relocalization for laparoscopic sequences," in *Robotics and Automation (ICRA), 2011 IEEE International Conference on*, pp. 4816–4821, IEEE, 2011.
- [2] B. Lin, A. Johnson, X. Qian, J. Sanchez, and Y. Sun, "Simultaneous tracking, 3d reconstruction and deforming point detection for stereo-scope guided surgery," in *Augmented Reality Environments for Medical Imaging and Computer-Assisted Interventions*, pp. 35–44, Springer, 2013.
- [3] R. Mur-Artal, J. M. M. Montiel, and J. D. Tardos, "Orb-slam: a versatile and accurate monocular slam system," *IEEE Transactions on Robotics*, vol. 31, no. 5, pp. 1147–1163, 2015.
- [4] N. Mahmoud, I. Cirauqui, A. Hostettler, C. Doignon, L. Soler, J. Marescaux, and J. Montiel, "Orbslam-based endoscope tracking and 3d reconstruction," in *International Workshop on Computer-Assisted and Robotic Endoscopy*, pp. 72–83, Springer, 2016.
- [5] N. Mahmoud, A. Hostettler, T. Collins, L. Soler, C. Doignon, and J. Montiel, "Slam based quasi dense reconstruction for minimally invasive surgery scenes," *arXiv preprint arXiv:1705.09107*, 2017.
- [6] M. Turan, Y. Almalioglu, H. Araujo, E. Konukoglu, and M. Sitti, "A non-rigid map fusion-based direct slam method for endoscopic capsule robots," *International journal of intelligent robotics and applications*, vol. 1, no. 4, pp. 399–409, 2017.
- [7] L. Chen, W. Tang, N. W. John, T. R. Wan, and J. J. Zhang, "Slam-based dense surface reconstruction in monocular minimally invasive surgery and its application to augmented reality," *Computer methods and programs in biomedicine*, vol. 158, pp. 135–146, 2018.
- [8] A. Marmol, A. Banach, and T. Peynot, "Dense-arthrosclam: dense intra-articular 3d reconstruction with robust localization prior for arthroscopy," *IEEE Robotics and Automation Letters*, 2019.
- [9] R. W. Sumner, J. Schmid, and M. Pauly, "Embedded deformation for shape manipulation," *ACM Transactions on Graphics (TOG)*, vol. 26, no. 3, p. 80, 2007.
- [10] T. Whelan, R. F. Salas-Moreno, B. Glocker, A. J. Davison, and S. Leutenegger, "Elasticfusion: Real-time dense slam and light source estimation," *The International Journal of Robotics Research*, vol. 35, no. 14, pp. 1697–1716, 2016.
- [11] J. Song, J. Wang, L. Zhao, S. Huang, and G. Dissanayake, "Dynamic reconstruction of deformable soft-tissue with stereo scope in minimal invasive surgery," *IEEE Robotics and Automation Letters*, vol. 3, no. 1, pp. 155–162, 2018.
- [12] R. A. Newcombe, D. Fox, and S. M. Seitz, "Dynamicfusion: Reconstruction and tracking of non-rigid scenes in real-time," in *Proceedings of the IEEE Conference on Computer Vision and Pattern Recognition*, pp. 343–352, 2015.
- [13] M. Innmann, M. Zollhöfer, M. Nießner, C. Theobalt, and M. Stamminger, "Volumedeform: Real-time volumetric non-rigid reconstruction," in *European Conference on Computer Vision*, pp. 362–379, Springer, 2016.
- [14] M. Dou, S. Khamis, et al., "Fusion4d: real-time performance capture of challenging scenes," *ACM Transactions on Graphics (TOG)*, vol. 35, no. 4, p. 114, 2016.
- [15] K. Guo, F. Xu, T. Yu, X. Liu, Q. Dai, and Y. Liu, "Real-time geometry, albedo, and motion reconstruction using a single rgb-d camera," *ACM Transactions on Graphics (TOG)*, vol. 36, no. 3, p. 32, 2017.
- [16] M. Dou, P. Davidson, S. R. Fanello, S. Khamis, A. Kowdle, C. Rhamann, V. Tankovich, and S. Izadi, "Motion2fusion: real-time volumetric performance capture," *ACM Transactions on Graphics (TOG)*, vol. 36, no. 6, p. 246, 2017.
- [17] A. Agudo, B. Calvo, and J. Montiel, "3d reconstruction of non-rigid surfaces in real-time using wedge elements," in *European Conference on Computer Vision*, pp. 113–122, Springer, 2012.
- [18] A. Petit and S. Cotin, "Environment-aware non-rigid registration in surgery using physics-based simulation," in *Asian Conference on Computer Vision (ACCV) Workshops*, 2018.
- [19] J. Lamarca and J. Montiel, "Camera tracking for slam in deformable maps," in *The European Conference on Computer Vision (ECCV) Workshops*, September 2018.
- [20] S. Thrun, W. Burgard, and D. Fox, *Probabilistic robotics*. MIT press, 2005.
- [21] N. Carlevaris-Bianco, M. Kaess, and R. M. Eustice, "Generic node removal for factor-graph slam," *IEEE Transactions on Robotics*, vol. 30, no. 6, pp. 1371–1385, 2014.
- [22] K. Eickenhoff, L. Paull, and G. Huang, "Decoupled, consistent node removal and edge sparsification for graph-based slam," in *2016 IEEE/RSJ International Conference on Intelligent Robots and Systems (IROS)*, pp. 3275–3282, IEEE, 2016.
- [23] J. Vallvé, J. Solà, and J. Andrade-Cetto, "Graph slam sparsification with populated topologies using factor descent optimization," *IEEE Robotics and Automation Letters*, vol. 3, no. 2, pp. 1322–1329, 2018.
- [24] J. Song, J. Wang, L. Zhao, S. Huang, and G. Dissanayake, "Mislam: Real-time large-scale dense deformable slam system in minimal invasive surgery based on heterogeneous computing," *IEEE Robotics and Automation Letters*, vol. 3, pp. 4068–4075, Oct 2018.
- [25] T. Igarashi, T. Moscovich, and J. F. Hughes, "As-rigid-as-possible shape manipulation," *ACM transactions on Graphics (TOG)*, vol. 24, no. 3, pp. 1134–1141, 2005.
- [26] O. Sorkine and M. Alexa, "As-rigid-as-possible surface modeling," in *Symposium on Geometry Processing*, vol. 4, pp. 109–116, 2007.
- [27] S. Giannarou, M. Visentini-Scarzanella, and G.-Z. Yang, "Probabilistic tracking of affine-invariant anisotropic regions," *IEEE transactions on Pattern Analysis and Machine Intelligence*, vol. 35, no. 1, pp. 130–143, 2013.